

To be published in Optics Letters:

Title: Disposable Opto-Acoustic Window Enabled Plug-and-Play Photoacoustic-Ultrasound Dual-modal Imaging
Authors: YUNHUI JIANG,FAN ZHANG,YUWEI ZHENG,RUIXI SUN,XIRAN CAI,Fei Gao
Accepted: 12 June 25
Posted 13 June 25
DOI: <https://doi.org/10.1364/OL.565354>

© 2025 Optica

OPTICA
PUBLISHING GROUP

Disposable Opto-Acoustic Window Enabled Plug-and-Play Photoacoustic-Ultrasound Dual-modal Imaging

YUNHUI JIANG¹, FAN ZHANG¹, YUWEI ZHENG¹, RUIXI SUN¹, XIRAN CAI^{1,*}, AND FEI GAO^{2,3,4,*}

¹Hybrid Imaging System Laboratory, School of Information Science and Technology, ShanghaiTech University, 393 Middle Huaxia Road, Shanghai, 201210

²School of Biomedical Engineering, Division of Life Sciences and Medicine, University of Science and Technology of China, Hefei, Anhui, 230026, China

³Suzhou Institute for Advanced Research, University of Science and Technology of China, Suzhou, Jiangsu, 215123, China

⁴School of Engineering Science, University of Science and Technology of China, Hefei, Anhui, 230026, China

*Corresponding author: fgao@ustc.edu.cn

*Corresponding author: caixr@shanghaitech.edu.cn

Compiled May 30, 2025

Photoacoustic imaging (PAI) and ultrasound imaging (USI) are important biomedical imaging techniques, due to their unique and complementary advantages in tissue's structure and function visualization. In this Letter, we propose a plug-and-play photoacoustic-ultrasound dual-modal imaging system (PnP-PAUS) with disposable opto-acoustic window (OAW). This OAW allows part of light to go through it, and another part of light to be converted to US transmission signal by PA effect. By single laser pulse illumination, both PA signals and reflected US signals can be generated. Then, a linear array probe receives both PA and US signals, enabling simultaneous dual-modal PA and US imaging. Phantom experiments were conducted involving pencil lead, hair, and plastic tube with black spot, as well as *in vivo* experiment on human finger. The US signals generated by the OAW reached a cross-correlation coefficient of 0.988 with the signals from a commercial single-point probe. The stable cross-correlation coefficient between the laser-induced ultrasound signals over 1460 s is above 0.968. The system's resolutions for PA and US imaging are 215 μm and 91 μm , with signal-to-noise ratios for PA and US signals reached up to 37.48 dB and 29.75 dB, respectively, proving the feasibility of the PnP-PAUS dual-modal imaging. The proposed PnP-PAUS system with disposable OAW provides an immediate and cost-effective approach to enable US imaging capability based on an existing PA imaging system.

PAI, a non-invasive biomedical imaging technique based on the photoacoustic effect, reveals endogenous chromophores (such as hemoglobin and melanin) and exogenous contrast agents (such as metal nanoparticles and organic molecules) by generating ultrasound signals through transient thermoelastic expansion induced by laser excitation. High-resolution images are reconstructed normally using delay-and-sum (DAS) algorithms [1–5]. Photoacoustic tomography (PAT) can achieve sub-millimeter resolution at depths of several centimeters, providing the optical contrast and functional imaging of tissues [6]. USI, on the other hand, acquires anatomical information of tissues through the propagation of sound waves and their reflection at interfaces with different acoustic impedances. The two imaging modalities offer complementary strengths in terms of anatomical and functional imaging [7].

Traditional PAUS dual-modal imaging systems often integrate an external ultrasound transmission module into a PA imaging system, which usually suffers higher cost, complex synchronization design, and un-coaxial light/sound illumination [8–12]. In this Letter, we propose plug-and-play photoacoustic-ultrasound (PnP-PAUS) dual-modal imaging with disposable opto-acoustic window (OAW). A conceptual illustration of the OAW is shown in Fig.1(a), which enables simultaneous light/sound illumination by a single pulsed laser. Specifically, part of the laser energy is transmitted through the window to illuminate the imaging target, the other part of the laser energy is absorbed by the optical absorber patterned on the window [13–16]. The unique advantage of OAW is its feasibility of generating custom-designed ultrasound transmission field at extremely low cost. Such simple and low-cost feature of OAW also enables its disposable usage for switching different OAW for different imaging scenarios.

In this work, we designed the OAW module by sticking a black tape on a glass slide, which can be flexibly positioned in front of the laser output. The experimental setup is shown in Fig. 1(b). Unlike previous studies that employed polydimethylsiloxane (PDMS)-based composite absorbers [13, 17–20], we em-

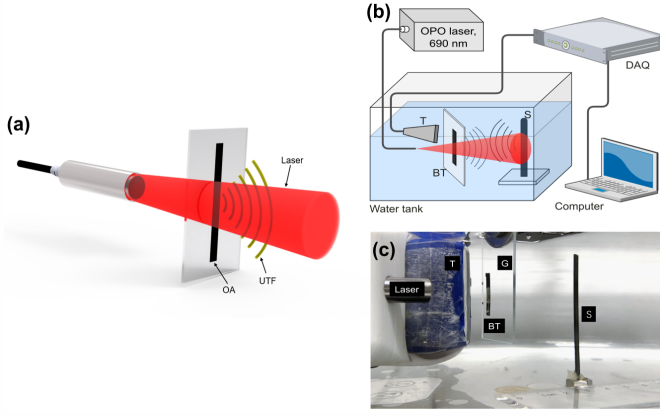


Fig. 1. (a) The conceptual illustration of OAW enabling laser illumination and ultrasound transmission field. (b) Experimental setup of PnP-PAUS system. (c) Photograph of PnP-PAUS system. OA, Optical absorber; UTF, Ultrasound transmission field; DAQ, Data Acquisition Card; T, Transducer; S, Sample; G, Glass.

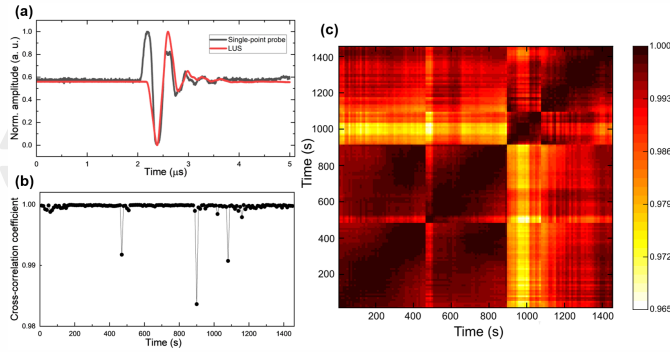


Fig. 2. Uniformity and stability analysis of the OAW module. (a) Comparison of LUS signal with ultrasound signal generated by a commercial single-point probe. (b) Cross-correlation coefficient of neighboring LUS signals versus variation with time. (c) Cross-correlation coefficient matrix of 146 sets of LUS signals over 1460 s.

ployed black tape as a more convenient and disposable optical absorber. To optimize laser energy utilization, the width of the black tape is designed to be smaller than the diameter of the laser beam. The black PVC tape used in the experiment was 20 mm in length, 3 mm in width, 0.13 mm in thickness, and could withstand a maximum temperature of 80 °C. The laser incident diameter near the window is 8 mm and the pulse width is 10 ns. The output laser energy per pulse is ~ 85 mJ. After partial absorption by the black tape, the energy reaching the skin surface was reduced to 39 mJ, resulting in a fluence of 12.42 mJ/cm², which complies with the ANSI safety limit[21]. It employs a pulsed laser (OPOpai-NIR1, TsingPAI Technology, Pte Ltd., China) with a wavelength of 690 nm and a repetition rate of 10 Hz as the light source.

Due to significant optical absorption of the black tape, it generates a strong laser-induced ultrasound (LUS) signal based on PA effect. In the experiment, both the transmitted laser through the 1-mm-thick glass, and the LUS signal generated by the black tape, propagate through water. The round-trip LUS signal reflects off the object's surface, together with the single-trip PA sig-

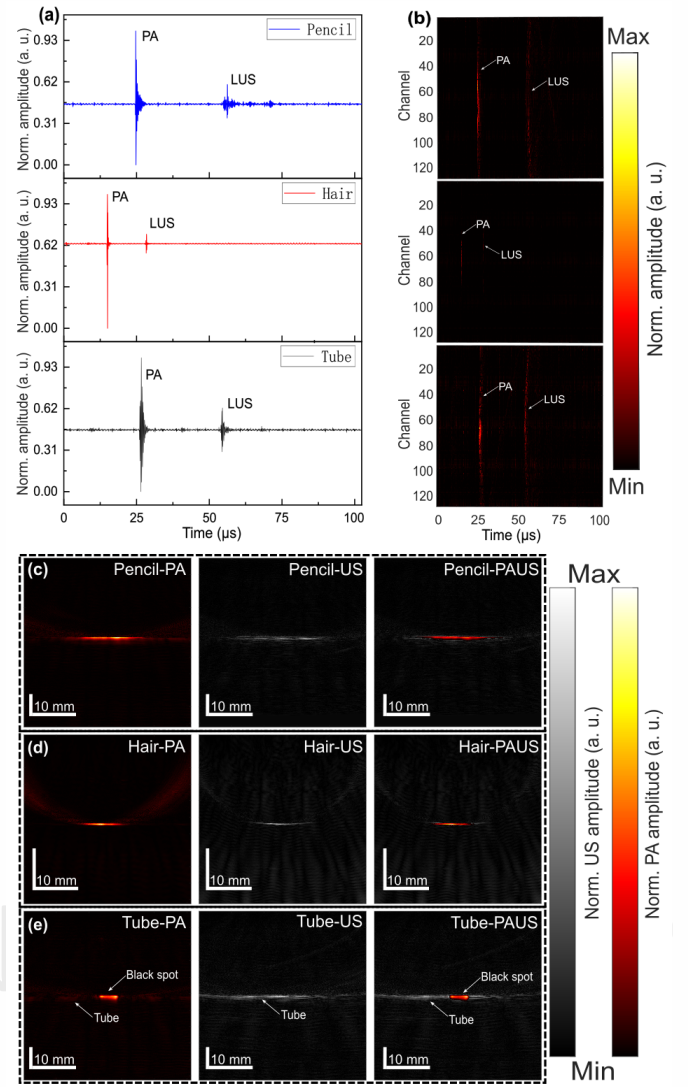


Fig. 3. (a) The received PA and US signals from pencil lead, hair, and a tube with black dot. (b) The sinogram images of the three phantoms mentioned above. (c)-(e) The PA, US, and PA-US imaging results of the three phantoms.

nals generated by the object through PA effect [22]. Compared to the commonly used transmission-based imaging methods [2, 13, 23], the proposed system employs a reflection-based configuration, as this design offers greater flexibility for practical applications. These reflected signals are ultimately received by a linear array probe with a central frequency of 7.5 MHz. The signals are acquired at a sampling rate of 40 MSPS using a high-speed data acquisition card (HISonics, HIS PATech Pte. Ltd.) with a total of 4096 sampling points, which are transmitted in real-time to a computer for image reconstruction using a conventional DAS algorithm. The photograph of the experimental setup is illustrated in Fig. 1(c).

To verify the uniformity and stability of the LUS signals generated by the OAW module, we irradiated the black tape continuously for 1460 s using the pulsed laser. A commercial single-point probe (Immersion Probe I2.25P6NF-H, Doppler Inc., China) with a center frequency of 2.25 MHz generates a pulsed signal that mimics the characteristics of a pulsed laser-excited LUS signals. The pulse signal has a repetition rate of 100 kHz,

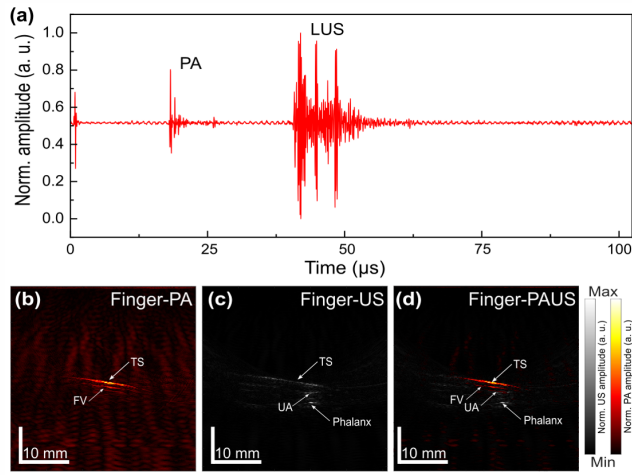


Fig. 4. (a) The received photoacoustic and ultrasound signals from the finger. (b)-(d) The PA, US, and PA-US imaging results of the finger. TS, tissue surface; FV, finger vasculature; UA, the upper aponeurosis.

a rising edge of 10.0 ns, and a duty cycle of 0.160%. Fig. 2(a) demonstrates the LUS signal generated by the black tape. The waveforms generally match very well, whose cross-correlation coefficient between the two signals reaches 0.988. This indicates that the LUS signal generated by the black tape is highly similar to the ultrasound signal generated by the commercial single-point probe.

In order to analyze the deformation of the LUS signals over time, we used the commercial single-point probe to collect the LUS signals at a distance of ~ 2 mm from the black tape during a continuous laser irradiation of 1460 s. One set of data was recorded every 10 s of irradiation, and a total of 146 sets of data were recorded. Fig. 2(b) demonstrates a cross-correlation analysis of the LUS signals generated at adjacent times of the black tape [24]. Under continuous laser irradiation for 1460 s, the signals showed only three deformations and the change in the number of cross-correlation coefficient was within 0.02. Fig. 2(c) shows the cross-correlation coefficient of signals at different times within 1460 s, where a minimum value of 0.968 is achieved between the signals at 500 s and 1010 s. The variation of the cross-correlation coefficient remains within 0.04, demonstrating the sufficient stability of the LUS signal.

To validate the feasibility of PnP-PAUS dual-modal imaging system, we used phantoms including a 2-mm-diameter pencil lead, a 0.07-mm-diameter human hair, and a 5.2-mm-diameter white plastic tube with black spot. Fig. 3(a) displays the generated PA and reflected US signals from these phantoms. The waveforms reveal two distinct signal peaks in time domain, with the US signal's propagation time approximately twice that of the PA signal. This difference arises because, in PAI, the laser's propagation time in water is negligible, and only single-trip propagation of the received PA signal is considered. In contrast, US signal involves round-trip propagation time for both transmission and receiving.

Fig. 3(b) presents the sinogram images of PA and US signals, illustrating the distribution of signals captured by different channels of the linear probe over the sampling period. Due to the higher laser intensity at the central part, both PA and US signal's intensity is also concentrated at the center of the US probe and along the laser beam path. Additionally, the signal

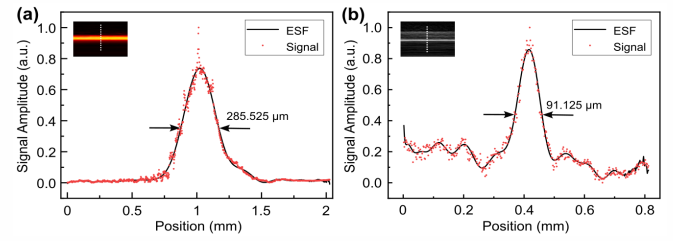


Fig. 5. Evaluation of the resolution of the PnP-PAUS system: (a) resolution for photoacoustic imaging of a hair. (b) The resolution for ultrasound imaging of the pencil lead. ESF, edge spread function.

intensity of the US signal is obviously lower than that of the PA signal, which is caused by the fact that US signal propagates in the form of a spherical wave. The three phantoms also have a small cross-section, and the distance between these phantoms and the tape is relatively long in comparison to the cross-section of the phantom, which results in weaker US signals reflected.

Fig. 3(c)-(e) show the reconstructed images of PA, US, and their overlapped PAUS dual-modal images. For the pencil lead phantom, both PAI and USI clearly delineate the shape and edges of the pencil lead. However, a notable difference exists in the measured lengths: the PA image shows approximately 2.3 cm, while the US image measures around 3.84 cm. This difference arises from the distinct signal generation and propagation mechanisms. The laser, acting as a point source, excites PA signals only in a localized region, limiting the visible structure in PAI. In contrast, US waves, generated by the black tape, propagate spherically, covering a larger area and reflecting more structural information. This demonstrates the better capability of recovering morphological information of USI. The PA image shows that pencil lead's length is approximately 2.3 cm, while the US image shows its length is roughly 3.84 cm. This demonstrates the better capability of recovering morphological information of USI.

To further evaluate the feasibility of the proposed PnP-PAUS system for *in vivo* biomedical imaging, we performed dual-modal imaging on the fingers of healthy volunteers, as depicted in Fig. 4. The finger is an ideal subject for PAUS dual-modal imaging because it includes both vascular and bones, which are optimal endogenous contrast for PA and US imaging, respectively. Additionally, given the high prevalence and significant clinical impact of finger arthritis, this also holds important clinical relevance [25]. In Fig. 4(a), the PA signal was first detected by the linear probe at 17.75 μ s, while the LUS signal was received after 22.71 μ s.

Table 1. The signal-to-noise ratio of the PA/US signals for the four phantoms in the experiment.

Unit: dB	Pencil lead	Hair	Tube	Finger
PA	31.73	37.48	32.27	23.48
US	20.15	23.44	22.89	29.75

Fig. 4(b)-(d) illustrate the reconstructed images of PAI and USI. In Fig. 4(b), the PA imaging clearly reveals the skin surface and vascular structures of the finger, indicating high optical absorption properties of the skin and blood vessels, though the PA contrast for the bone is relatively low. Fig. 4(c) shows high

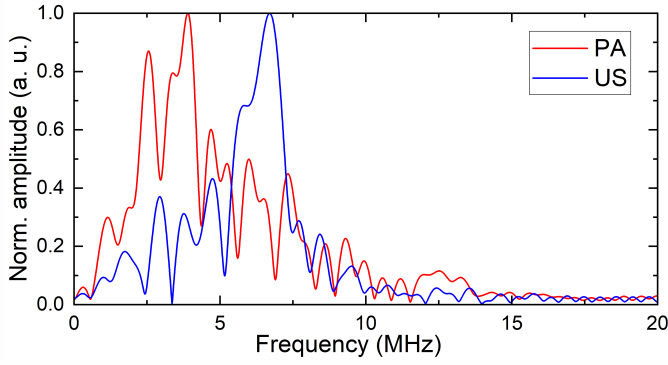


Fig. 6. The normalized frequency spectrum of PA and US signals of the finger signal.

acoustic contrast of the bone relative to surrounding tissues through US imaging, effectively outlining the surface contours of the deep subcutaneous finger bone. When PA and US images are fused, as shown in Fig. 4(d), the relative positions of the finger's vascular and bony structures are distinctly visible.

In order to delineate the system's resolution, we analyzed the edge response for photoacoustic and ultrasound imaging of a hair strand and a pencil lead. As shown in Fig. 5, the normalized experimental data were fitted using the edge spread function (ESF, black solid line). The full width at half maximum (FWHM) of the ESF, minus the diameter of the phantom, was used to represent the system's resolution. We observed that for imaging a 70 μm hair strand, the resolution of photoacoustic imaging was approximately 215 μm . For imaging a 2 mm pencil lead, the resolution of the ultrasound imaging was 91.125 μm . Although measurements at different positions along the phantom edge may slightly vary, and the performance of image reconstruction algorithm can influence resolution, this demonstrates that the PnP-PAUS system is capable of identifying small objects with high resolution.

$$\text{SNR(dB)} = 10 \cdot \log_{10} \left(\frac{A_{\text{signal}}}{A_{\text{noise}}} \right)^2 \quad (1)$$

To characterize the quality of PA and US signals generated by the system, we calculated the signal-to-noise ratio (SNR) using Eq. 1, where A_{signal} and A_{noise} represent the amplitudes of the time-domain signal and noise, respectively. Both signals were extracted over the same data length for analysis. The measured distances from the OAW to the pipe, pencil lead, and finger were 3 cm, while the hair was positioned 2 cm away. These distances were chosen based on the optimal PA imaging performance demonstrated by our proposed system. The results are shown in Table 1. The SNR of both US and PA signals exceed 20 dB in phantom and *in vivo* finger experiments, demonstrating the high signal quality of the proposed PnP-PAUS system.

We also evaluated the signal's frequency spectrum of the PnP-PAUS system on *in vivo* finger. As shown in Fig. 6, the power spectral density of both PA and US signals falls within 8 MHz. For PA and US signals, the primary peak of the spectrum is situated at 3.9 MHz and 6.7 MHz, respectively. Therefore, when PA and US signals cannot be separated in the time domain, appropriate band-pass filtering can be used, such as low-pass filtering for PA signals and high-pass filtering for US signals.

In this letter, we propose a Plug-and-Play photoacoustic-ultrasound dual-modal imaging system with disposable OAW.

This system enables stable PA and US imaging based on single-pulse excitation by simply incorporating a very cheap OAW slide. The standardized fabrication of the OAW slide ensures consistent performance, demonstrating sufficient system reliability. When PA and US signals cannot be separated in the time domain, they can be distinguished using appropriate band-pass filtering. Reflection-induced artifacts in photoacoustic imaging systems can degrade image fidelity. Being different from previous works that treat surface absorption induced ultrasound reflection as artifacts [26–28], we propose to enhance such absorption by employing an OAW to enable dual-modal imaging. Further optimization of OAW to exploit the broadband nature of photoacoustic signals is desired to enhance ultrasound imaging depth and resolution [29]. In the future work, improvements can be achieved including the incorporation of fiber-optic beam-splitting to enable multi-angle illumination, replacement of linear transducers with bowl-shaped spherical array to enable real-time 3D imaging, and custom-patterned OAW to optimize ultrasound transmission for high-performance US imaging.

Disclosures. The authors declare no conflicts of interest.

REFERENCES

1. M. Xu and L. V. Wang, Rev. Sci. Instruments **77**, 041101 (2006).
2. Y. Zhao, S. Wang, J. Merrill, *et al.*, Opt. letters **45** **7**, 1703 (2020).
3. D. Jiang, L. Zhu, S. Tong, *et al.*, J. Biomed. Opt. **29** (2023).
4. J. Weber, P. C. Beard, and S. E. Bohndiek, Nat. Methods **13**, 639 (2016).
5. D. Nozdriukhin, S. K. Kalva, Çağla Özsoy, *et al.*, Adv. Sci. **11** (2023).
6. L. V. Wang and S. Hu, Science **335**, 1458 (2012).
7. J. F. Havlice, N. D. Jon, and Taenzer, Proc. IEEE **67**, 620 (1979).
8. W. Kim, W.-S. Choi, J. Ahn, *et al.*, Opt. letters **48** **2**, 343 (2023).
9. C. Lee, S. Cho, D. Lee, *et al.*, Photoacoustics **31** (2023).
10. J. Yuan, G. Xu, Y. Yu, *et al.*, J. Biomed. Opt. **18** (2013).
11. N. Nyayapathi, E. Zheng, Q. Zhou, *et al.*, Front. photonics **5** (2024).
12. M. Gerling, Y. Zhao, S. Nania, *et al.*, Theranostics **4**, 604 (2014).
13. D. Thompson, J. R. Nagel, D. Gasteau, and S. Manohar, Photoacoustics **25** (2021).
14. M. C. Finlay, C. A. Mosse, R. J. Colchester, *et al.*, Light. Sci. & Appl. **6** (2017).
15. K. Pham, S. Noimark, N. Huynh, *et al.*, IEEE Trans. on Ultrason. Ferroelectr. Freq. Control. **68**, 1007 (2020).
16. T. F. Fehm, X. L. Deán-Ben, and D. Razansky, Appl. Phys. Lett. **105**, 173505 (2014).
17. D. Thompson, D. Gasteau, and S. Manohar, Photoacoustics **18**, 100154 (2020).
18. W.-Y. Chang, W. Huang, J. Kim, *et al.*, Appl. Phys. Lett. **107** (2015).
19. L. Shi, Y. Jiang, F. R. Fernandez, *et al.*, Light. Sci. & Appl. **10**, 143 (2021).
20. H. W. Baac, J. G. Ok, A. Maxwell, *et al.*, Sci. reports **2**, 989 (2012).
21. A. N. S. Institute, American National Standard for Safe Use of Lasers (Laser Institute of America, 2022). Standard.
22. J. L. Johnson, K. van Wijk, and M. Sabick, Ultrasound Med. & Biol. **40**, 513 (2014).
23. S. Ermilov, R. Su, A. Conjusteau, *et al.*, Ultrason. imaging **38**, 77 (2016).
24. D. Wang, S. K. Sahoo, X. Zhu, *et al.*, Nat. communications **12**, 3150 (2021).
25. J. Jo, C. Tian, G. Xu, *et al.*, Photoacoustics **12**, 82 (2018).
26. M. Kuniyil Ajith Singh and W. Steenbergen, Photoacoustics **3**, 123 (2015).
27. H. N. Y. Nguyen, A. Hussain, and W. Steenbergen, Biomed. optics express **9** **10**, 4613 (2018).
28. D. Allman, A. Reiter, and M. A. L. Bell, IEEE Trans. on Med. Imaging **37**, 1464 (2018).
29. L. Wang, Y. Zhao, B. Zheng, *et al.*, Sci. Adv. **9** (2023).

FULL REFERENCES

1. M. Xu and L. V. Wang, "Photoacoustic imaging in biomedicine," *Rev. Sci. Instruments* **77**, 041101 (2006).
2. Y. Zhao, S. Wang, J. Merrill, *et al.*, "Triplex radiometric, photoacoustic, and ultrasonic imaging based on single-pulse excitation," *Opt. letters* **45** 7, 1703–1706 (2020).
3. D. Jiang, L. Zhu, S. Tong, *et al.*, "Photoacoustic imaging plus x: a review," *J. Biomed. Opt.* **29** (2023).
4. J. Weber, P. C. Beard, and S. E. Bohniek, "Contrast agents for molecular photoacoustic imaging," *Nat. Methods* **13**, 639–650 (2016).
5. D. Nozdriukhin, S. K. Kalva, Çağla Özsoy, *et al.*, "Multi-scale volumetric dynamic optoacoustic and laser ultrasound (oplus) imaging enabled by semi-transparent optical guidance," *Adv. Sci.* **11** (2023).
6. L. V. Wang and S. Hu, "Photoacoustic tomography: In vivo imaging from organelles to organs," *Science* **335**, 1458 – 1462 (2012).
7. J. F. Havlice, N. D. Jon, and Taenzer, "Medical ultrasonic imaging: An overview of principles and instrumentation," *Proc. IEEE* **67**, 620–641 (1979).
8. W. Kim, W.-S. Choi, J. Ahn, *et al.*, "Wide-field three-dimensional photoacoustic/ultrasound scanner using a two-dimensional matrix transducer array," *Opt. letters* **48** 2, 343–346 (2023).
9. C. Lee, S. Cho, D. Lee, *et al.*, "Panoramic volumetric clinical handheld photoacoustic and ultrasound imaging," *Photoacoustics* **31** (2023).
10. J. Yuan, G. Xu, Y. Yu, *et al.*, "Real-time photoacoustic and ultrasound dual-modality imaging system facilitated with graphics processing unit and code parallel optimization," *J. Biomed. Opt.* **18** (2013).
11. N. Nyayapathi, E. Zheng, Q. Zhou, *et al.*, "Dual-modal photoacoustic and ultrasound imaging: from preclinical to clinical applications," *Front. photonics* **5** (2024).
12. M. Gerling, Y. Zhao, S. Nania, *et al.*, "Real-time assessment of tissue hypoxia in vivo with combined photoacoustics and high-frequency ultrasound," *Theranostics* **4**, 604 – 613 (2014).
13. D. Thompson, J. R. Nagel, D. Gasteau, and S. Manohar, "Laser-induced ultrasound transmitters for large-volume ultrasound tomography," *Photoacoustics* **25** (2021).
14. M. C. Finlay, C. A. Mosse, R. J. Colchester, *et al.*, "Through-needle all-optical ultrasound imaging in vivo: a preclinical swine study," *Light. Sci. & Appl.* **6** (2017).
15. K. Pham, S. Noimark, N. Huynh, *et al.*, "Broadband all-optical plane-wave ultrasound imaging system based on a fabry-perot scanner," *IEEE Trans. on Ultrason. Ferroelectr. Freq. Control.* **68**, 1007–1016 (2020).
16. T. F. Fehm, X. L. Deán-Ben, and D. Razansky, "Four dimensional hybrid ultrasound and optoacoustic imaging via passive element optical excitation in a hand-held probe," *Appl. Phys. Lett.* **105**, 173505 (2014).
17. D. Thompson, D. Gasteau, and S. Manohar, "Spatially compounded plane wave imaging using a laser-induced ultrasound source," *Photoacoustics* **18**, 100154 (2020).
18. W.-Y. Chang, W. Huang, J. Kim, *et al.*, "Candle soot nanoparticles-polydimethylsiloxane composites for laser ultrasound transducers," *Appl. Phys. Lett.* **107** (2015).
19. L. Shi, Y. Jiang, F. R. Fernandez, *et al.*, "Non-genetic photoacoustic stimulation of single neurons by a tapered fiber optoacoustic emitter," *Light. Sci. & Appl.* **10**, 143 (2021).
20. H. W. Baac, J. G. Ok, A. Maxwell, *et al.*, "Carbon-nanotube optoacoustic lens for focused ultrasound generation and high-precision targeted therapy," *Sci. reports* **2**, 989 (2012).
21. A. N. S. Institute, *American National Standard for Safe Use of Lasers* (Laser Institute of America, 2022). Standard.
22. J. L. Johnson, K. van Wijk, and M. Sabick, "Characterizing phantom arteries with multi-channel laser ultrasonics and photo-acoustics," *Ultrasound Med. & Biol.* **40**, 513–520 (2014).
23. S. Ermilov, R. Su, A. Conjusteau, *et al.*, "Three-dimensional optoacoustic and laser-induced ultrasound tomography system for preclinical research in mice: design and phantom validation," *Ultrason. imaging* **38**, 77–95 (2016).
24. D. Wang, S. K. Sahoo, X. Zhu, *et al.*, "Non-invasive super-resolution imaging through dynamic scattering media," *Nat. communications* **12**, 3150 (2021).
25. J. Jo, C. Tian, G. Xu, *et al.*, "Photoacoustic tomography for human musculoskeletal imaging and inflammatory arthritis detection," *Photoacoustics* **12**, 82–89 (2018).
26. M. Kuniyil Ajith Singh and W. Steenbergen, "Photoacoustic-guided focused ultrasound (pafusion) for identifying reflection artifacts in photoacoustic imaging," *Photoacoustics* **3**, 123–131 (2015).
27. H. N. Y. Nguyen, A. Hussain, and W. Steenbergen, "Reflection artifact identification in photoacoustic imaging using multi-wavelength excitation," *Biomed. optics express* **9** 10, 4613–4630 (2018).
28. D. Allman, A. Reiter, and M. A. L. Bell, "Photoacoustic source detection and reflection artifact removal enabled by deep learning," *IEEE Trans. on Med. Imaging* **37**, 1464–1477 (2018).
29. L. Wang, Y. Zhao, B. Zheng, *et al.*, "Ultrawide-bandwidth high-resolution all-optical intravascular ultrasound using miniaturized photoacoustic transducer," *Sci. Adv.* **9** (2023).